[1]Elham Shahidi

[2]* Abdolhamid Ansari

[3]Amirhossein Kohsari

Identifying Porphyry Copper Alterations in the Chehel Kureh Area Using Deep Learning Techniques on PRISMA Hyperspectral Imagery

Journal of Electrical Systems

Abstract: This study employs deep learning methods based on spectral-spatial features to identify alterations associated with porphyry deposits in the Chehel Kureh copper area, one of the richest and least-studied copper mines in Iran. Porphyry deposits are of significant importance in the mining industry due to their high potential for copper production, and the related alterations (including argillic, phyllic, and propylitic alterations) play a crucial role in their exploration and identification. In this research, hyperspectral data from the PRISMA satellite were utilized, which, due to its diverse spectral bands, can provide detailed information about surface materials; however, accurate classification of these data faces challenges due to severe spectral variability and environmental impacts such as cloud cover and shadows.

To address this challenge, three deep learning methods were investigated: three-dimensional convolutional neural networks (3D CNN), a hybrid method combining 3D CNN with support vector machines (SVM), and a hybrid method combining three-dimensional wavelet transformation with SVM. The results indicated that the 3D CNN method performed best in identifying and classifying alterations associated with porphyry deposits, achieving an overall accuracy of 94%. The hybrid 3D CNN and SVM method performed slightly lower, with an accuracy of 93%. Finally, the hybrid method combining three-dimensional wavelet transformation and SVM demonstrated lower accuracy compared to the other two methods. This study illustrates that the use of 3D convolutional neural networks can be an effective approach to address classification issues in hyperspectral images like those from PRISMA, thereby enhancing the identification of mineral alterations.

Keywords: Porphyry deposits, copper alteration, deep learning, three-dimensional convolution, SVM, three-dimensional wavelet transformation, hyperspectral images, Chehel Kureh mine, PRISMA hyperspectral data.

I. INTRODUCTION

Porphyry copper deposits (PCDs) play a crucial role in global copper production, serving as one of the most important sources of this metal. (Sillitoe 2010, Singer 2017)These deposits are significant not only because of their vast mineral volumes but also due to the complex and systematic patterns of hydrothermal alteration they exhibit.(Sillitoe 2010, Neal, Wilkinson et al. 2018) Alteration systems associated with these deposits typically include potassic, phyllic (sericitic), propylitic, and argillic alterations, each observed in different areas of the deposit.(Lowell and Guilbert 1970, Sillitoe 2010, Peyghambari, Zhang et al. 2024)

These zonations are essential for both identifying deposits and assessing their economic potential.(Bedini and Chen 2020, Peyghambari, Zhang et al. 2024) Potassic alteration, occurring in the central zone, is commonly associated with minerals such as potassium feldspar and biotite, often encompassing economically viable deposits of copper and gold.(Lowell and Guilbert 1970, Sillitoe 2010, Neal, Wilkinson et al. 2018, Peyghambari, Zhang et al. 2024) The phyllic alteration in the intermediate zone is characterized by the presence of minerals like muscovite, quartz, and pyrite, making it a key indicator of these systems.(Lowell and Guilbert 1970, Sillitoe 2010, Neal, Wilkinson et al. 2018, Peyghambari, Zhang et al. 2024)In the outer regions, argillic alteration manifests through clay minerals such as kaolinite and illite, which may overlap with propylitic alteration marked by minerals like chlorite and epidote. .(Lowell and Guilbert 1970, Sillitoe 2010, Neal, Wilkinson et al. 2018, Peyghambari, Zhang et al. 2024) These alteration patterns are vital for exploration and mining studies due to their strong correlation with mineralization areas.(Heller Pearlshtien, Pignatti et al. 2021)

Hyperspectral imaging technology serves as a crucial tool for identifying and analyzing hydrothermal alterations.(Sorrentino, Chirico et al. 2024) Its remarkable ability to extract precise spectral information allows for the effective identification of the unique characteristics of minerals associated with hydrothermal processes. (Graham, Kokaly et al. 2018, Bedini and Chen 2020, Peyghambari, Zhang et al. 2024, Sorrentino, Chirico et al. 2024)Each mineral possesses a specific spectral signature that corresponds to molecular vibrations such as Fe^{2+}, Fe^{3+}, Al-OH, Mg-OH, and OH^{-}.(Harraden, Mcnulty et al. 2013, Fu, Cheng et al. 2023)For instance, muscovite displays a strong absorption band

[1] Ph.D. Candidate, Yazd University

[2] Associate Professor, Yazd University

[3] Associate Professor, Faculty of Mining and Metallurgy, Yazd University

* Corresponding author

around 2.2 micrometers, linked to hydroxyl and aluminum groups within its structure. (Harraden, Mcnulty et al. 2013, Fu, Cheng et al. 2023) In contrast, kaolinite exhibits distinct absorption bands at approximately 1.4 and 2.2 micrometers, corresponding to OH groups. (Harraden, Mcnulty et al. 2013, Fu, Cheng et al. 2023) The vibrations of OH-Fe and OH-Mg in the chlorite structure generate absorption bands within the range of 2.25 to 2.35 micrometers, while epidote shows absorption bands at around 1.4 and 2.35 micrometers (Harraden, Mcnulty et al. 2013, Fu, Cheng et al. 2023) . These spectral signatures provide a foundation for the precise identification of minerals and facilitate the mapping of alteration zones in hyperspectral data(Cao, Yao et al. 2020, Heller Pearlshtien, Pignatti et al. 2021). The Chehel Kureh deposit, due to its economic significance and high copper grade, is recognized as one of the most important copper mines in Iran.(Maanijou, Rasa et al. 2008) This deposit is notable not only for its vast mineral reserves but also for its unique geological features, making it of great interest in economic geology. (Maanijou, Rasa et al. 2008)Located in the Lonka mountain range, it lies at the boundary between the Lut Block and the Eastern Flysch Zone of Iran, characterized by various types of alteration.(Maanijou, Rasa et al. 2008) The Chehel Kureh mining area, structurally connected to the Lut Block, is influenced by tectonic activity and fault movements(Maanijou, Rasa et al. 2008) and comprises sedimentary, metamorphic, and volcanic rocks(Tirrul, Bell et al. 1983).

This paper explores advanced methods for identifying hydrothermal alterations in the Chehel Kureh deposit using hyperspectral imaging data from the PRISMA satellite. Three approaches are evaluated: the use of three-dimensional convolutional neural networks (3D CNN), a hybrid model combining 3D CNN with a support vector machine (SVM), and a hybrid approach based on three- dimensional discrete wavelet transform (3D-DWT) and SVM.Hyperspectral images (HSI) have become powerful tools for analyzing and classifying surface features due to their high spectral resolution and ability to analyze complex spectral structures.(Zhang, Zhao et al. 2020, Li, Wang et al. 2024) However, hyperspectral data pose several challenges, including data redundancy, increased information volume, and reduced classification efficiency, primarily due to their high dimensionality and significant correlation between bands.(Li, Zhang et al. 2017, Zhang, Zhao et al. 2020, Wu, Al-qaness et al. 2024) Moreover, traditional classification methods, which predominantly rely on spectral information, often suffer from insufficient accuracy due to issues such as limited sample sizes and the Hughes phenomenon where the dimensionality of the data increases without a corresponding increase in training samples.(Li, Zhang et al. 2017, Wu, Al-qaness et al. 2024) Additionally, the lack of utilization of the spatial information present in these images further diminishes the effectiveness of these methods.(Li, Zhang et al. 2017, Zhang, Zhao et al. 2020, Wu, Al-qaness et al. 2024)

In recent years, to address the challenges of hyperspectral image processing particularly the high dimensionality and strong band correlation the use of deep learning methods has significantly increased. (Praveen and Menon 2020, Zhang, Zhao et al. 2020, Peyghambari, Zhang et al. 2024)One of the most efficient approaches is 3D Convolutional Neural Networks (3D CNNs), which play a pivotal role in improving hyperspectral data classification due to their ability to simultaneously extract complex spectral and spatial features. (Praveen and Menon 2020, Zhang, Zhao et al. 2020, Peyghambari, Zhang et al. 2024) By utilizing 3D filters, these networks can effectively exploit the cubic structure of hyperspectral data and capture the spectral-spatial correlations within. This capability is especially impactful in areas such as the analysis of hydrothermal alteration zones associated with porphyry copper deposits.(Peyghambari, Zhang et al. 2024)

In this study, a novel approach based on the combination of 3D Convolutional Neural Networks (3D CNN) and Support Vector Machine (SVM) has been explored. This hybrid approach leverages the best features of both models, with the 3D CNN serving as a feature extractor for complex spectral and spatial attributes, and the SVM acting as the final classifier, using these features to achieve higher accuracy and improved generalization capability.(Chen, Yang et al. 2020) In the 3D CNN-SVM model, the output of the convolutional layers of the 3D CNN, which contains valuable spectral-spatial information, is fed into the Support Vector Machine instead of the standard network output layer.(Chen, Yang et al. 2020) By utilizing these extracted features, the SVM significantly enhances the model's accuracy and performance.(Chen, Yang et al. 2020)Additionally, in this study, another approach based on the combination of 3D Discrete Wavelet Transform (3D-DWT) and SVM has been utilized. Hyperspectral data, which consist of hundreds of narrow bands, offer a high potential for extracting multiple features. The 3D-DWT, by simultaneously decomposing spectral and spatial information, has the capability to extract spatial-spectral components from the images. The features extracted by 3D-DWT are then used as input to the SVM, and ultimately, this combined method leads to a significant improvement in classification performance.(Anand, Veni et al. 2021)

Geology of the Study Area

The Chehel Kureh copper deposit is located 120 kilometers northwest of Zahedan, in the Lonka mountain range(Maanijou 2007, Maanijou, Rasa et al. 2008), and is part of the eastern Iran flysch zone, commonly known as the Nahbandan-Khash zone(Maanijou, RASAE et al. 2009)This zone is characterized by thick flysch deposits, including shale, sandstone, siltstone, and limestone, which overlie an ophiolitic basement associated with the oceanic crust (Tirrul, Bell et al. 1983).The Nehbandan-Khash zone has undergone significant evolutionary transitions from oceanic crust to continental crust, thereby forming a component of the young Tethys During the Late Cretaceous period, the Lut and Afghan blocks were separated by an intercontinental ocean(Tirrul, Bell et al. 1983).

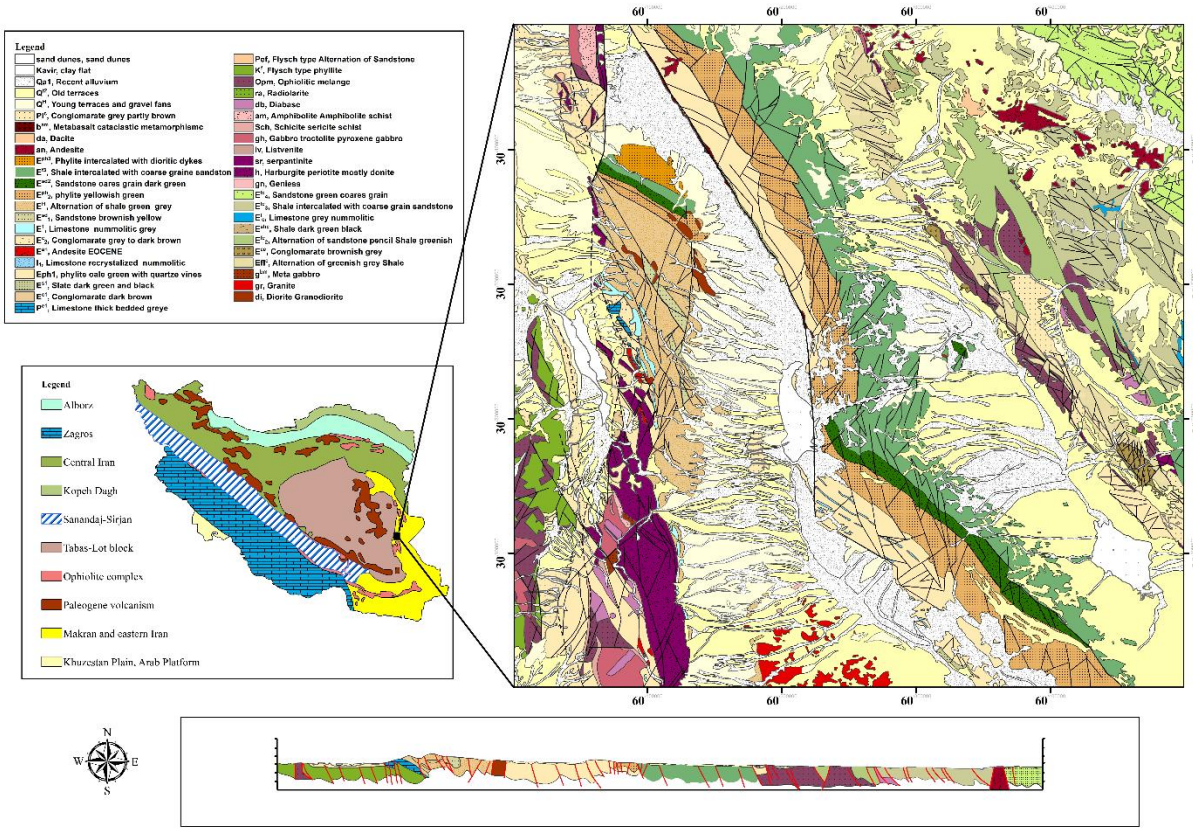

Figure 1. (A) Geological map of Iran, scale 1:100,000, Sheet No. 8050. (B) Structural zones map of Iran based on Stocklin's classification.

The ocean, which served as the source of the region's ophiolites, closed during the Campanian period and is recognized as a forearc basin that was filled until the mid-EoceneThe collision between the Lut and Afghan blocks resulted in the folding and uplift of this basin(Stöcklin, Eftekharnezhad et al. 1972). Additionally, both intrusive and extrusive magmatic activities have significantly influenced the sedimentary units, contributing to the formation of the Zahedan-Nehbandan magmatic belt (Camp and Griffis 1982). Due to the abundant presence of ophiolites, this zone is referred to as the "Kald Melange Zone" and is acknowledged as the welded zone of Sistan situated between the Lut and Afghan block(Stöcklin, Eftekharnezhad et al. 1972).In the region, volcanic rock outcrops, diabase, and ultrabasic rocks are observed in lens-shaped formations(Stöcklin, Eftekharnezhad et al. 1972). Additionally, slight metamorphism has occurred in the surrounding rocks of Zahedan, with ages estimated to range from 15 to 83 million years based on potassium-argon dating, which is consistent with the age of the region's ophiolites(Delaloye and Desmons 1980, Maanijou 2007). The oceanic basin that formed during the Cretaceous period integrated the Lut and Afghan blocks during the Senonian, and absolute age data ranging from 60 to 100 million years obtained from the ophiolites south of Nasratabad corroborates this event(Delaloye and Desmons 1980, Maanijou 2007). The flysch deposits in this zone underwent folding during the Neogene period, with granitic intrusions such as the Zahedan-Khash and Mirabad granites penetrating these layers(Berberian and Berberian 1981, Maanijou 2007). The host rocks of the Chehel Kureh deposit consist of graywacke, siltstone, shale, and calcareous sandstone, characterized by an Eocene-aged flysch (turbiditic) facies(Maanijou 2007). Fine-grained limestones occur as large, lens-shaped, and isolated bodies in the western and northwestern sections of the deposit(Maanijou 2007).

Wall rock alteration, a common process in hydrothermal deposits, in the Chehel Kureh deposit comprises chloritic, carbonate (ankerite, siderite, and dolomite), kaolinitic, silicic, sericitic (minor amounts), and sulfide alterations(Maanijou, Rasa et al. 2008, Maanijou, RASAE et al. 2009). These alterations, which can manifest as surface halos, are indicative of possible subsurface mineralization(Maanijou, Rasa et al. 2008, Maanijou, RASAE et al. 2009). Alterations associated with intrusive bodies in the Chehel Kureh deposit predominantly include silicic, carbonate, chloritic, and kaolinitic types, often occurring as vein-type structures and occasionally as more pervasive alterations(Maanijou, Rasa et al. 2008, Maanijou, RASAE et al. 2009).Mining activities in the Chehel Kureh area date back approximately 1100 to 1300 years(Maanijou, Rasa et al. 2008). In addition to this deposit, the region also hosts other mines, such as Porchangi and Abkandi. The Chehel Kureh deposit is of significant economic importance and is unique from a geological-economic perspective in Iran(Maanijou, Rasa et al. 2008). Figure 1 shows the geological map of the study area and its location on the structural zones map of Iran based on Stocklin's classification. Figure 1 shows the geological map of the study area at a scale of 1:100,000, as well as its position in the structural zones of Iran, based on Stocklin's classification.

II. MATERIALS AND METHODS

PRISMA Data Characteristics

The PRISMA (PRecursore IperSpettrale della Missione Applicativa, Hyperspectral Precursor of the Application Mission) hyperspectral imaging satellite of the Italian Space Agency was launched into orbit on March 22, 2019 with 29 days revisiting time(Loizzo, Daraio et al. 2019).PRISMA is categorized as a small-size satellite, encompassing both hyperspectral imaging capabilities and a mediumresolution panchromatic imager(Habashi, Moghadam et al. 2024). The PRISMA hyperspectral sensor, which shares the same name as the satellite mission, utilizes prisms to capture the dispersion of incoming energy using the "Pushbroom" image scanning technique(Habashi, Moghadam et al. 2024).

Table 1. PRISMA payloads' main characteristics. The first column reports the requirements, while the last three specify the sensor performance as derived by the Leonardo Company and reported by (Loizzo, 2019)

	Requirements	**VNIR**	**SWIR**	**PAN**
Spectral range	$400-2500nm$	$400-1010nm$		
Spectral resolution (FWHM)	$<15nm$	$9-13nm$		
Spectral bands		66	171	1
SNR	≥ 160 $-200(400-450nm)$ $\geq 200(450-1000nm)$ $\geq 200(1000-1750nm)$ $\geq 100(1950-2350)$ $\geq 100(PAN)$	161 $-209(1000$ $-1300nm)$ $100(1950-2350nm)$	380 $-800(1000-1300nm)$ 200 $-400(1500-1750nm)$ 100 $-200(1950-2350nm)$	191
Absolute radiometric accuracy	$\leq 5\%$	$\leq 5\%$	$\leq 5\%$	$\leq 5\%$
Swath width			$30km; 2.27^{\circ}$	
Ground sampling distance (GSD)		30m	30m	5m
Orbital altitude		620km		

The captured hyperspectral images comprise 239 bands ranging from visible/near-infrared (VNIR) to shortwave infrared (SWIR), with 66 bands within the VNIR range and 173 bands within the SWIR range. Additionally, nine bands are captured in the overlapping wavelength region of VNIR and SWIR. These images offer a spatial coverage of 30 km × 30 km with a spatial resolution of 30 m. The spectral separation among the bands is less than 12 nm. Furthermore, the panchromatic imagery is provided at a 5 m spatial resolution(Spiller, Carbone et al. 2023). PRISMA data is freely available for research purposes through the Italian Space Agency(Spiller, Carbone et al. 2023) .The hyperspectral and panchromatic data are provided in HDF5 format, with specifications outlined in Table 3, and delivered at four processing levels(Spiller, Carbone et al. 2023, Esmaeili, Fathianpour et al. 2024).PRISMA products are divided into four levels, each with unique characteristics presented in Table 2. In this study, a Level 2D PRISMA dataset has been used, which corresponds to Top-of-Atmosphere Radiance that has been radiometrically corrected and calibrated into physical units. Therefore, surface data do not need to be corrected for atmospheric interactions(Habashi, Moghadam et al. 2024) .

In this research, two 2D-level processed PRISMA hyperspectral images of the Chehel Koreh region were utilized to identify and map the alterations associated with porphyry copper deposits. These images, acquired on August 12, 2023 (PRS_L2D_STD_20230812064712_20230812064717_0001) and December 23, 2024 (PRS_L2D_STD_20241223065032_20241223065037_0001), were obtained from the official portal of the Italian Space Agency (ASI).

Table 2. Description of PRISMA different level correction(Spiller, Carbone et al. 2023, Esmaeili, Fathianpour et al. 2024).

Level	corrections
Level 1 1	(Hyperspectral / PAN) - radiometrically corrected and calibrated radiance data in physical units. • Top-of Atmosphere Spectral Radiance • Cloud mask • Sun-glint Mask • Calibration and • characterization data used • Classification Mask.
Level 2B	Geolocated at Bottom-of-Atmosphere Radiance.

Level 2C	Geolocated At-surface Reflectance Product (Hyperspectral / PAN). This product includes: • Aerosol Characterization Product (VNIR) • Water Vapour Map Product (Hyperspectral) • Cloud Characterization.
Level 2D	geocoded version of the level 2C products (Hyperspectral / PAN).

Data and Dataset

In this study, we utilized hyperspectral data from PRISMA to identify alterations related to porphyry copper in the study area. The dataset consists of 180 sampling points, with spectra obtained in the laboratory and classified according to mineral type and associated alteration type.The minerals examined include calcite, chlorite, kaolinite, and muscovite, which were accurately identified based on spectral data and geological information.The UTM coordinates for the sampling points were collected from field data. These points were overlaid on the PRISMA hyperspectral image, with the alteration type specified for each location. Three main alteration types were identified and classified: kaolinitic alteration, chloritic alteration, and calcitic alteration.To enhance the visualization of the precise locations, the sampling points were displayed on an RGB image constructed from bands 126, 90, and 48 of the PRISMA dataset (Figure 2).

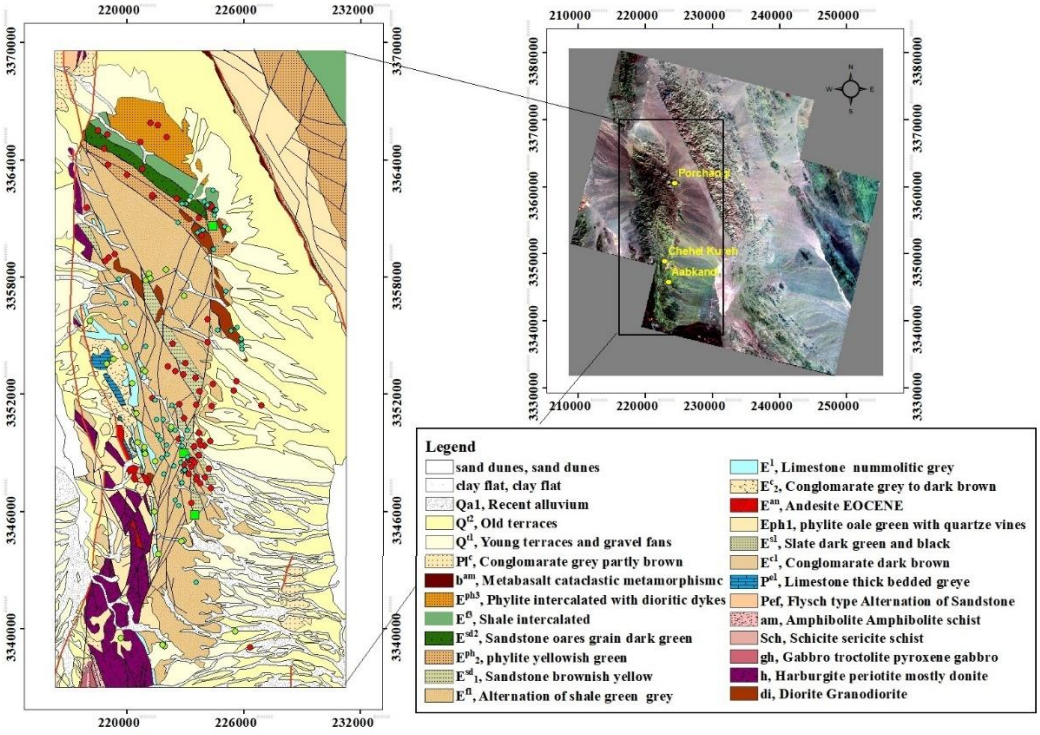

Figure 2: Location of sampling points overlaid on the RGB composite image of PRISMA data (bands 126, 90, and 48) and the geological map.

This specific combination of bands was selected for its higher resolution, which aids in distinguishing the sampling points and provides clearer representation of their locations within the image. Additionally, the sampling points were mapped on the geological map of the area to facilitate a more thorough analysis of their relationship with the geological features.For examining the spectral characteristics of the minerals, we presented the spectra extracted from the PRISMA image for muscovite, kaolinite, calcite, and chlorite. These spectra were compared with the resampled spectra from the USGS spectral library (Figure 3). This comparison aimed to deepen our understanding of the spectral behavior of each mineral and to visually assess how they align with the standard library spectra.

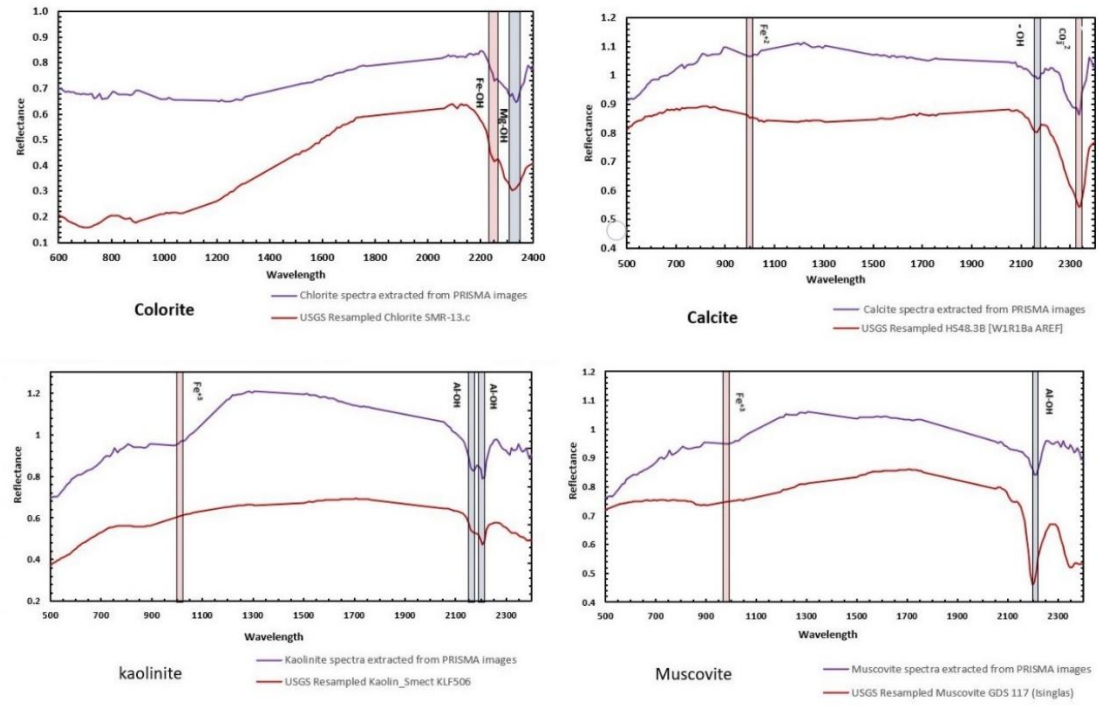

Figure 3: Comparison of the reflectance spectra extracted from the PRISMA image with the resampled mineral spectra from the USGS spectral library, including kaolinite, chlorite, calcite, and muscovite.

Methodology

Spatial-Spectral Approaches in Hyperspectral Image Classification

Hyperspectral imaging (HSI) has emerged as a pivotal tool in remote sensing, offering unparalleled spectral and spatial information that facilitates the comprehensive analysis of surface features.(Ahmad, Khan et al. 2020) By capturing detailed spectral signatures at the pixel level, HSI provides a unique "spectral fingerprint" for materials, enabling precise identification and differentiation of surface components. Typically operating across the 0.4 to 2.5 micrometer range, HSI sensors acquire data in narrow spectral bands, spanning from the visible to the short-wave infrared (SWIR) regions(Ahmad, Khan et al. 2020). This extensive spectral coverage proves invaluable for a wide array of applications, including natural resource management, environmental monitoring, and mineral exploration, where accurate material identification is critical(Ahmad, Khan et al. 2020).However, this technology presents specific challenges in the classification process. HSI images, due to their high dimensionality and significant intra-class variability, require more complex methods compared to traditional classification approaches. Common classification methods like KNN, SVM, and logistic regression, which heavily rely on spectral information and fail to preserve spatial features, do not perform well with this type of data. Another challenge is that HSI images, often constrained by sensor limitations and data complexity, typically have low spatial resolution, which reduces classification accuracy in many real-world applications.(Bera, Shrivastava et al. 2022)

To overcome these challenges, the combination of spectral and spatial information is essential. New methods such as Convolutional Neural Networks (CNNs) have replaced traditional methods due to their ability to extract spatial-spectral features. 3D CNN models process small 3D cubes of HSI data and use 3D kernels to analyze multiple adjacent bands, thereby preserving spectral information. This approach results in the extraction of more accurate feature maps, leading to improved classification outcomes(Ahmad, Khan et al. 2020, Spiller, Carbone et al. 2023).

In general, spatial-spectral classifiers can be divided into two categories: the first category examines spatial and spectral information separately before combining them, while the second category which includes deep learning-based methods such as CNNs and 3D wavelets processes both types of information simultaneously and extracts common features(Bera, Shrivastava et al. 2022).

The use of these advanced methods has yielded promising results in the field of hyperspectral image classification and has significantly reduced previous challenges(Bera, Shrivastava et al. 2022).On the other hand, deep learning models such as CNNs have achieved remarkable success compared to traditional classifiers, primarily due to the automation of the process for extracting high-level features from raw HSI data. This approach has demonstrated superior performance,

especially in cases where the data possess high dimensions and complexities, opening new horizons in the field of hyperspectral image classification(Bera, Shrivastava et al. 2022).

In this study, three spectral-spatial methods are used for hyperspectral image classification: 3D Convolutional Neural Networks (3D CNN), a combination of 3D CNN and SVM, and a combination of 3D Wavelet Transform and SVM. Each of these methods is specifically designed to extract and classify the spectral and spatial features of hyperspectral images. The schematic diagram in Figure 4 clearly displays the different stages of these methods.

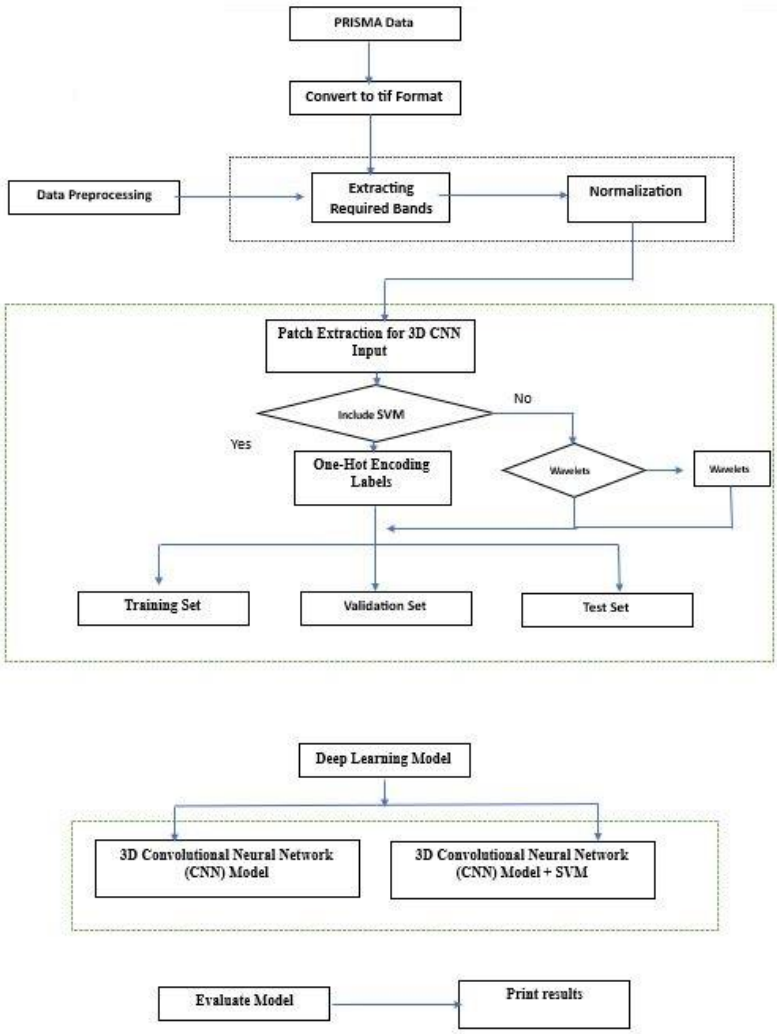

Figure 4: Schematic diagram of the three methods used in this study for hyperspectral image classification

3D Convolutional Neural Network (3D CNN) Model

The proposed model is based on a three-dimensional convolutional neural network (3D-CNN) that simultaneously extracts and analyzes the spatial and spectral features of hyperspectral data. The model's input consists of 3D patches of size 33×33×3 from the PRISMA data, which are processed in the first convolutional layer using 32 filters of size 3×3×3. This initial layer extracts basic spatial and spectral features. In the subsequent convolutional layers, with more filters (64 and 128), more complex and deeper features are extracted from the data.After each convolutional layer, 2×2×2 max pooling layers are applied to reduce the data size and improve the model's efficiency. Batch normalization is applied after each convolutional layer to accelerate learning and prevent overfitting. Additionally, dropout layers with a rate of 0.4 are included between the fully connected layers to mitigate overfitting by randomly deactivating some neurons during training.After the convolutional and pooling layers, the data is flattened into a one-dimensional vector and passed through fully connected layers with 1024 and 512 neurons. Finally, the output is classified into three alteration classes (Argillic, Phyllic, and Propylitic) using the Softmax activation function.The model utilizes the Cross-Entropy loss function for multi-class classification problems and the Adam optimizer with a learning rate of 0.001. The proposed algorithm illustrates the different stages of model processing in Figure 5, which includes 3D convolution layers, pooling, normalization, fully connected layers, and classification.

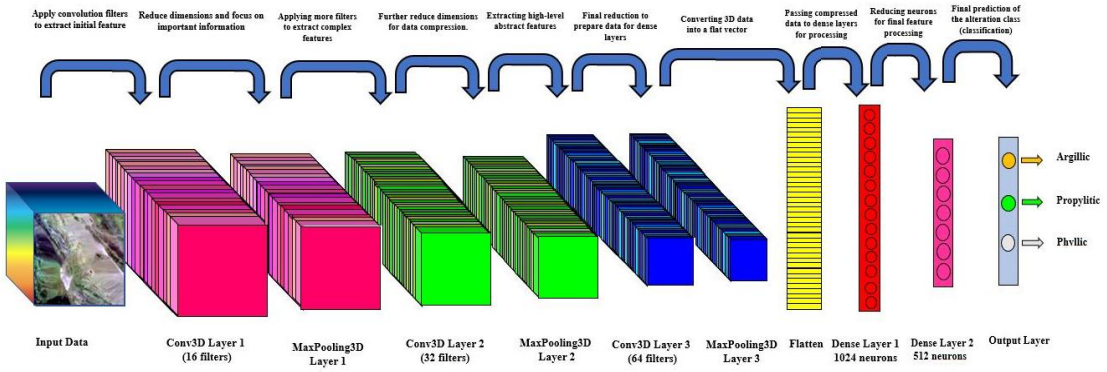

Figure 5. Three-dimensional convolutional neural networks (3D-CNN) framework for remotely sensed hyperspectral image (HSI) classification.

The results of the proposed model implementation are presented in Figures 6 and 7, demonstrating the effectiveness of the 3D convolution-based algorithm in accurately classifying and identifying alteration zones in PRISMA hyperspectral data. As a spectral-spatial classifier, the model simultaneously extracts both spatial and spectral features, enabling precise differentiation of alteration types. Figure 6 displays the final classification map for the first image, where Argillic, Phyllic, and Propylitic alteration zones are represented in distinct colors. Notably, overlapping alteration zones are clearly visible, highlighting the model's capability to identify complex structures and gradual changes in mineral compositions. Additionally, three separate grayscale images show the spatial distribution of each alteration type, with the model successfully and independently detecting these zones.

Figure 7 presents similar results for the second image, where the model has successfully identified and classified the alteration zones with high accuracy. As observed, the model efficiently distinguishes overlapping zones in both images. This ability to classify overlapping alteration zones is a key strength of the 3D convolution approach, as it simultaneously processes both spectral and spatial information, providing more accurate results when dealing with complex hyperspectral data.

These results emphasize that the 3D convolution method not only serves as a spectral-spatial classifier but also excels at handling overlapping alteration zones. The proposed algorithm demonstrates its effectiveness in processing and distinguishing complex patterns in hyperspectral data, underscoring its potential for more precise and efficient mineral exploration applications.

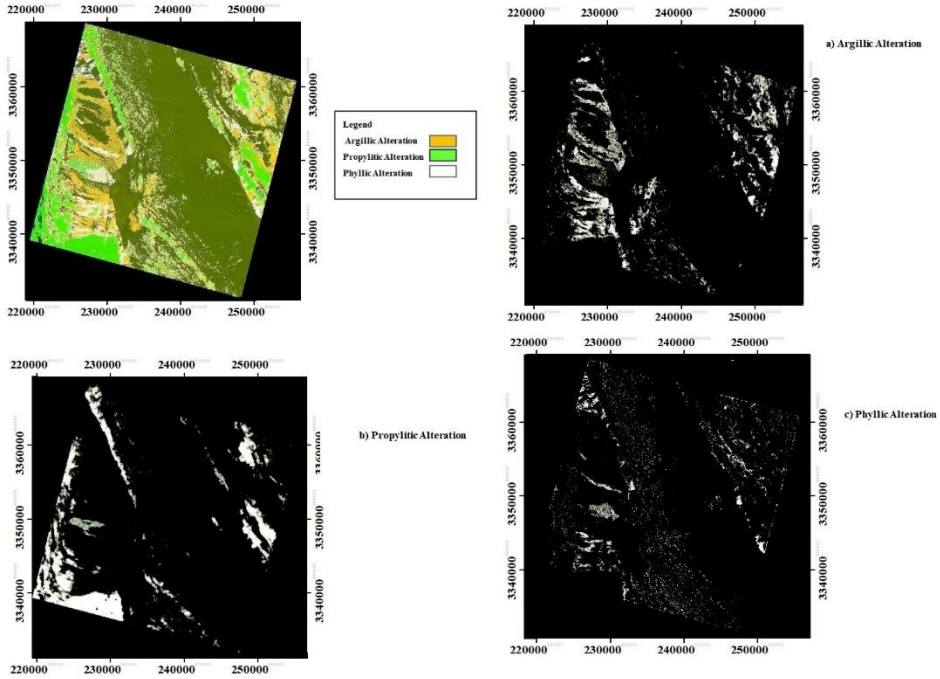

Figure 6: Final classification map for the PRISMA image PRS_L2D_STD_20230812064712_20230812064717_0001, illustrating the distribution of alteration zones. (a) Argillic alteration, (b) Propylitic alteration, and (c) Phyllic alteration, each shown separately in grayscale to highlight their spatial distribution. Overlapping regions indicate the model's capability in distinguishing complex spectral-spatial patterns.

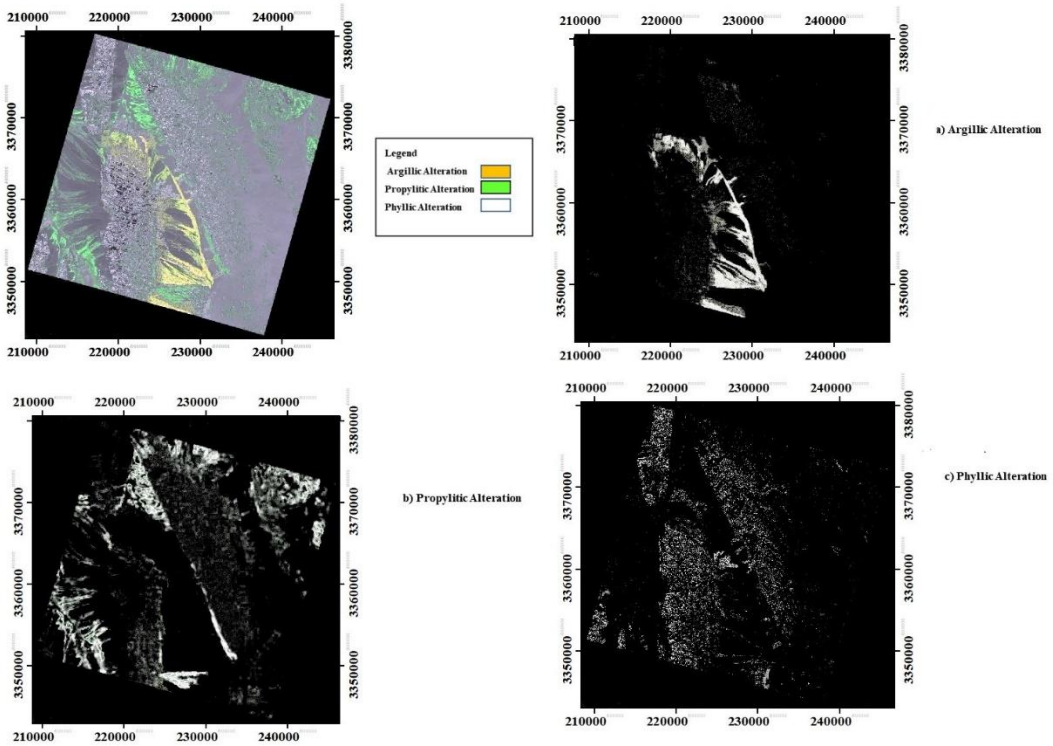

Figure 7: Final classification map for the PRISMA (PRS_L2D_STD_20241223065032_20241223065037_0001), illustrating the distribution of alteration zones. (a) Argillic alteration, (b) Propylitic alteration, and (c) Phyllic alteration, each shown separately in grayscale to highlight their spatial distribution. Overlapping regions indicate the model's capability in distinguishing complex spectral-spatial patterns.

3D Convolutional Neural Network and Support Vector Machine Model

In this study, a three-dimensional convolutional neural network (3D CNN) combined with a support vector machine (SVM) algorithm is used to identify alteration zones in hyperspectral data. Initially, the hyperspectral data is extracted into three-dimensional patches that encompass depth, height, and width along with the number of spectral bands. This approach enables the model to extract more complex features from the hyperspectral data (figure 8). The designed 3D CNN model includes the following layers:

- First 3D Convolutional Layer consists of 16 filters with a kernel size of (1, 3, 3) and a ReLU activation function. This layer aids in identifying initial patterns in the data. By utilizing small filters, this layer extracts local features such as edges and textures. The 'same' padding ensures that the output dimensions are equal to the input dimensions.

- Subsequently, a Batch Normalization Layer is added to the model, which helps improve the speed and stability of the learning process. By normalizing the inputs, the model can rapidly converge and avoid unwanted fluctuations.

- Next, a 3D Max Pooling Layer with a pooling size of (1, 2, 2) and 'same' padding is used to reduce the dimensionality of the features while retaining the maximum extracted features. This layer also helps decrease computations and prevent overfitting.

- The Second 3D Convolutional Layer consists of 32 filters with a kernel size of (1, 3, 3) and a ReLU activation function. This layer allows the model to extract more complex features from the data. By utilizing a greater number of filters, the model can learn additional patterns.

- Again, a Batch Normalization Layer and a 3D Max Pooling Layer similar to the previous layers are added to the model. Then, the Third 3D Convolutional Layer with 64 filters and a kernel size of (1, 3, 3) and a ReLU activation function is included as the last convolutional layer in the model, facilitating the extraction of advanced features.

- Finally, a Flatten Layer is designed to convert the three-dimensional output into a one-dimensional vector, enabling the model to utilize the extracted features for subsequent stages.

- After extracting features from this model, a support vector machine (SVM) with a linear kernel is employed for classifying the extracted features. This algorithm, trained on the extracted features, acquires the ability to identify different alterations in the hyperspectral data.

- The final model combines the strengths of deep neural networks and SVM to achieve more accurate identification of alteration zones in hyperspectral data, with the expectation of providing high accuracy in detecting various alteration regions.

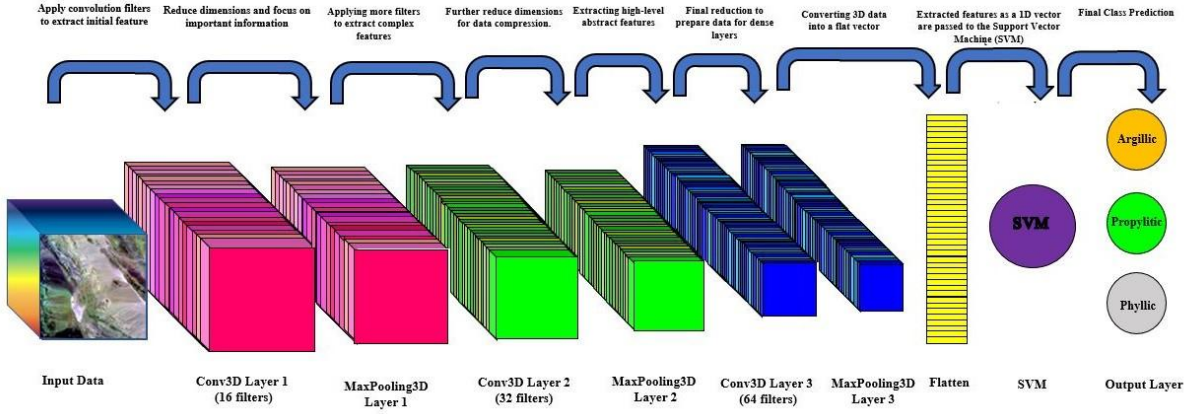

Figure 8: Framework of the combined 3D Convolutional Neural Network and Support Vector Machine (3D-CNN + SVM) method for hyperspectral image (HSI) classification.

The 3D CNN-SVM combined model was implemented on two PRISMA images, which cover the study area. The results demonstrate that the model effectively classifies alteration zones and extracts both spectral and spatial features.

Figures 9 and 10 show the classification results of these two images. The model successfully identified alteration zones of argillic, phyllic, and propylitic types with high accuracy. Notably, regions of overlap between different alteration types were clearly identified, highlighting the model's ability to capture complex spectral-spatial patterns.

In Figure 9, the classification map of the first image clearly delineates the alteration zones, with the spectral-spatial features of each class distinctly extracted. Additionally, black-and-white images of each alteration type (argillic, phyllic, and propylitic) display their spatial distribution. Similarly, Figure 10 presents the classification results of the second PRISMA image, where the model consistently and accurately identifies and classifies the alteration zones.

Overall, the 3D Convolutional Neural Network (3D CNN) outperformed in identifying and classifying alteration zones. It was able to extract more complex features from the spectral-spatial data and generally delivered higher accuracy in detecting various alteration types. However, in specific areas, the combined 3D CNN-SVM model performed better. This is due to the SVM algorithm's ability to more precisely separate the data, especially in areas where alterations appear overlapped or similar. In these regions, using SVM as the final classifier improved the accuracy in identifying similar or overlapping alteration zones. This performance difference in certain areas highlights the advantage of combining both methods to enhance the overall accuracy of the model.

The integration of 3D Convolutional Neural Networks for feature extraction and the SVM algorithm for final classification strengthens the overall power of this approach. By leveraging the deep learning capabilities of CNNs to extract complex features and the classification strength of SVMs, the model demonstrates excellent performance in identifying alteration zones in spectral-spatial data. The results indicate that this combined approach is effective for processing high-dimensional spectral-spatial data and represents a promising tool for mineral exploration and geological mapping.

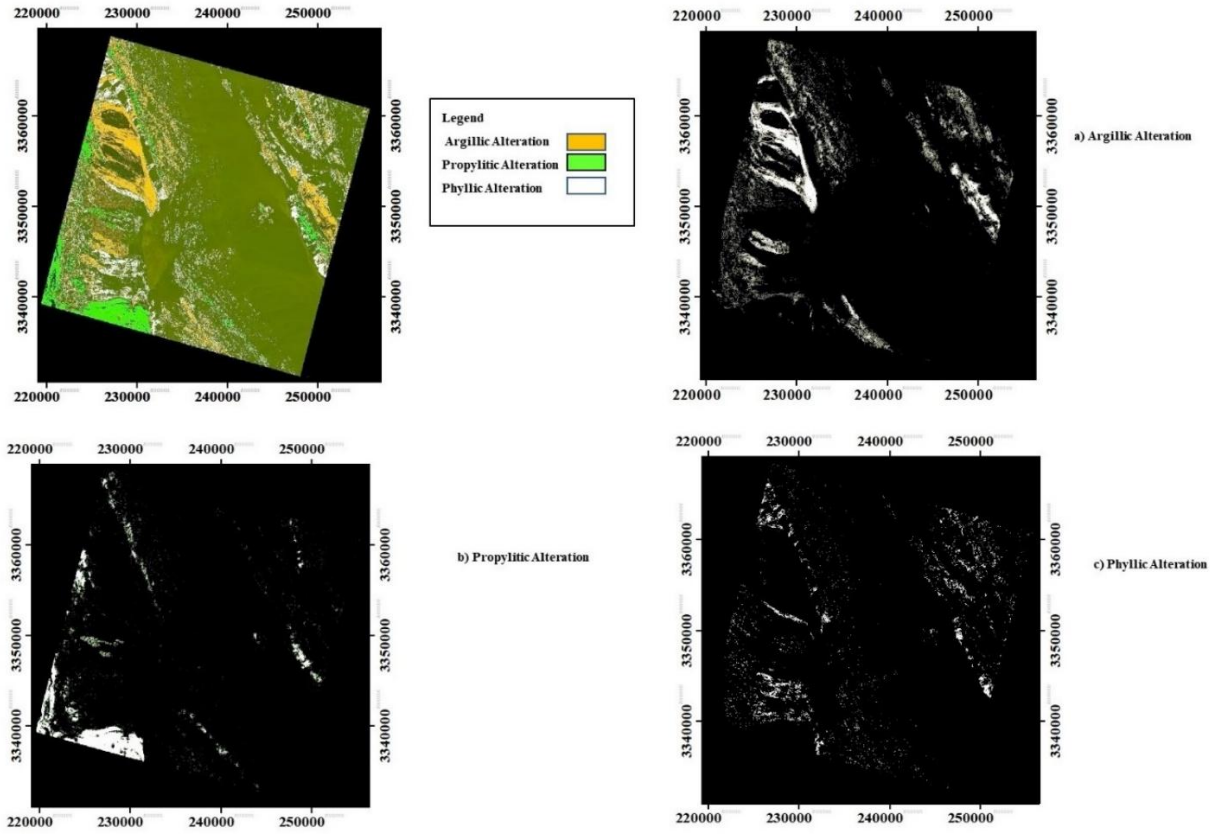

Figure 9: Classification map of the PRS_L2D_STD_20230812064712_20230812064717_0009 image, showing the identified alteration zones of argillic, phyllic, and propylitic types. Black-and-white images of each alteration type (argillic, phyllic, and propylitic) indicate their spatial distribution.

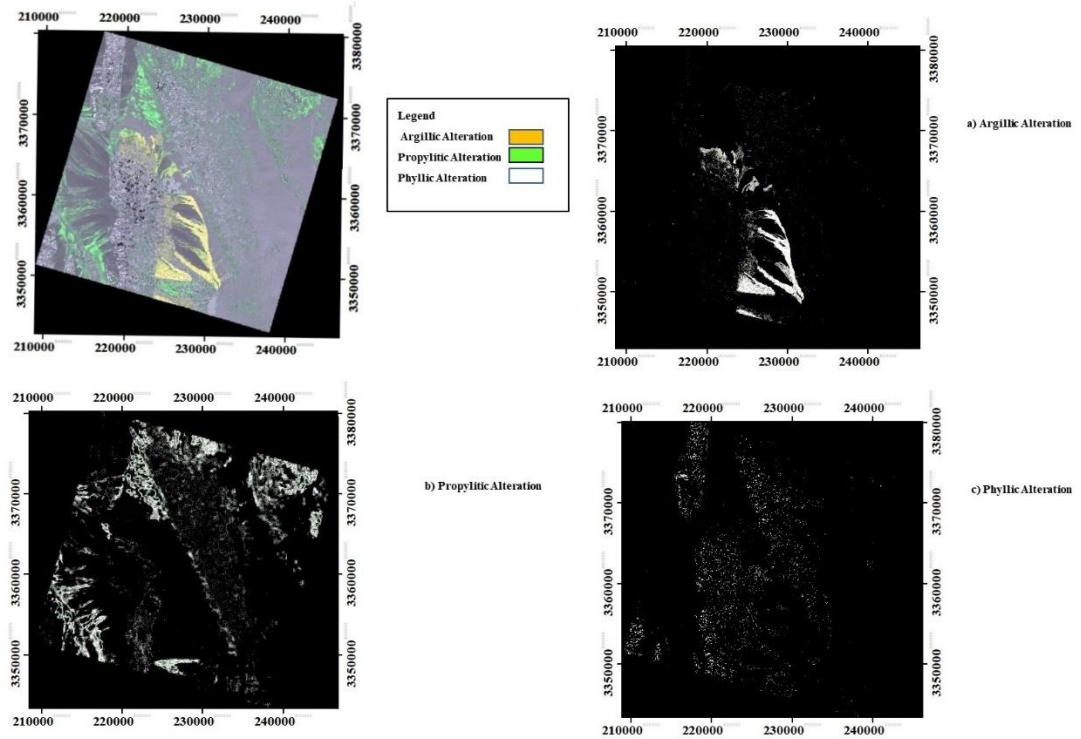

Figure 10: Classification map of the PRS_L2D_STD_20241223065032_20241223065037_00010010 image, showing the identified alteration zones of argillic, phyllic, and propylitic types. Black-and-white images of each alteration type (argillic, phyllic, and propylitic) indicate their spatial distribution.

3D Wavelet Transform and Support Vector Machine Hybrid Model

Wavelet Type

The wavelet used in this study is the Daubechies wavelet with the parameter db1. This type of wavelet is known for its mathematical properties and adaptability in signal and image analysis. The features of the wavelet employed in this research are used to extract information from hyperspectral data.

Thresholding

Thresholding is performed to identify different mineral alteration zones using specific bands. This thresholding aims to distinguish between Argillic, Phyllic, and Propylitic zones by defining specific ranges of absorption values for the corresponding bands. The different zones are defined as follows:

- Argillic Zone: Includes Kaolinite with absorptions of 2200, 2160, and 1000.
- Phyllic Zone: Includes Muscovite with an absorption of 2200.
- Propylitic Zone: Includes Chlorite with absorptions of 2313, 2335, and 2327.

Wavelet Functionality

The code used in this study performs wavelet transformation on three-dimensional patches (patches with depth, height, and width) using the extract_wavelet_features function. This process involves the following steps:

1. Decomposing patches into different levels and orientations and extracting wavelet coefficients.
2. Converting the obtained coefficients into a one-dimensional array for easier processing.
3. Utilizing the extracted wavelet features as input for the SVM classifier.

the various stages of the proposed method are illustrated in Figure 11 as a flowchart. This figure outlines different phases, including data preprocessing, spectral-spatial feature extraction using 3D CNN and wavelet transform, and final classification with SVM. The flowchart summarizes the entire (figure 11).

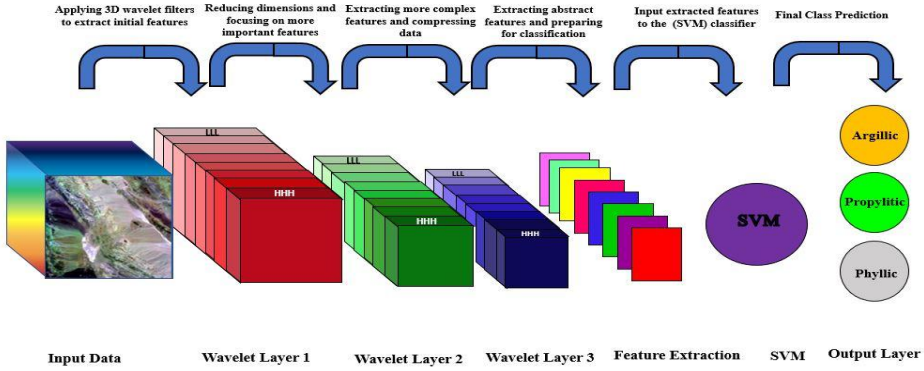

Figure 11: Workflow for PRISMA Data Processing and Classification Using 3D CNN and SVM Models. The process begins with data preprocessing, including band extraction and normalization. Data patches are then prepared for input into a 3D CNN, with an optional step to include SVM for classification. The model is trained, validated, and tested before final evaluation and result output. The combination of deep learning (3D CNN) and traditional machine learning (SVM) is used to enhance classification accuracy for alteration zones.

the model of 3D Wavelet Transform and Support Vector Machine (SVM) was applied to hyperspectral data captured by the Prisma satellite in 2023 and 2024. The results show that while the model was able to identify alteration zones, its performance was weaker compared to the two previously used methods, namely the 3D CNN and SVM-based models. Figure 12 illustrates the results of applying the algorithm to the image PRS_L2D_STD_20230812064712_20230812064717_0009.

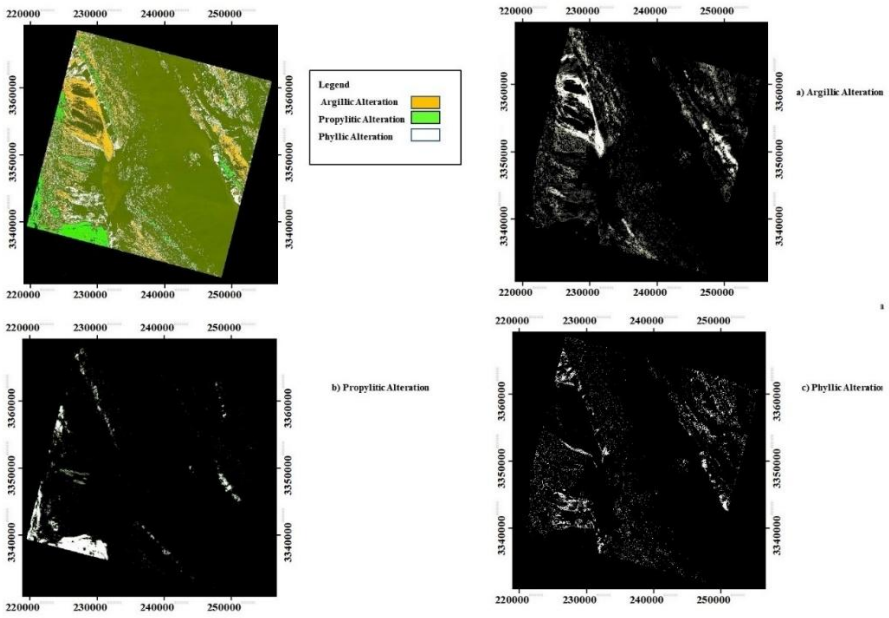

Figure 12: Results of applying the 3D Wavelet Transform and Support Vector Machine (SVM) algorithm on the image P PRS_L2D_STD_20241223065032_20241223065037_0001. The classification map reveals alteration zones identified with lower accuracy compared to CNN-based methods.

This classification map reveals that the identified alteration zones are less distinct compared to the CNN-based methods. Similarly, Figure 13 shows the results for the image PRS_L2D_STD_20241223065032_20241223065037_0001, where the model struggles to effectively differentiate between overlapping alteration zones. This highlights the limitations of the 3D Wavelet Transform and SVM method in handling complex spectral-spatial data Compared to the other two methods, this approach demonstrates weaker performance in distinguishing overlapping alteration zones or zones with similar spectral characteristics. Although the wavelet-SVM combination can still offer insights, its overall accuracy and precision are lower than those of the CNN-based methods.

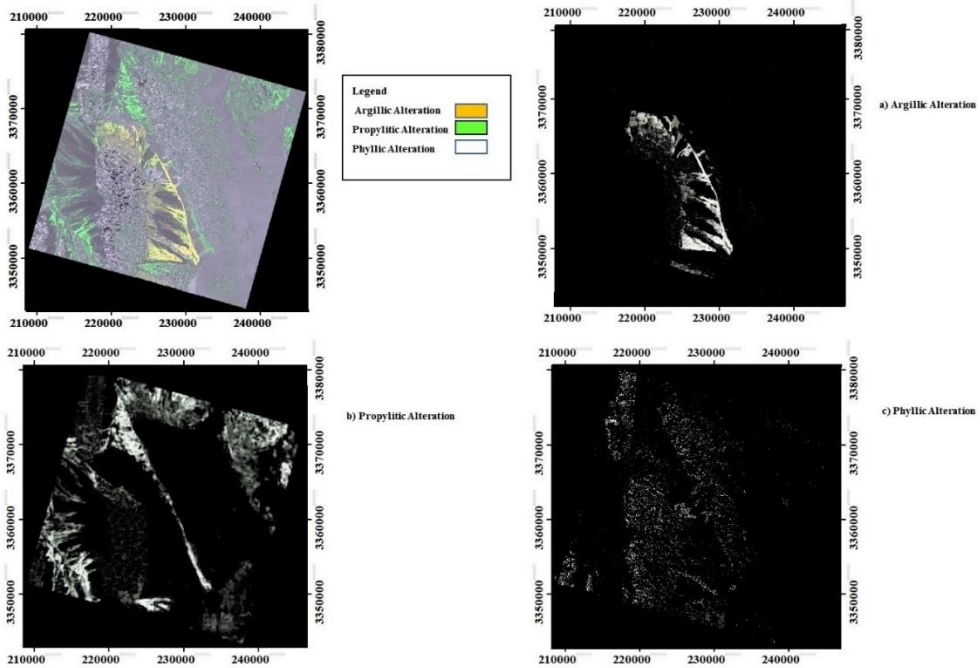

Figure 13: Results of applying the 3D Wavelet Transform and Support Vector Machine (SVM) algorithm on the image the PRS_L2D_STD_20241223065032_20241223065037_00010010 . The classification map shows overlapping alteration zones that are not well differentiated, highlighting the limitations of this method compared to CNN-based approaches.

Accuracy Statement

Confusion Matrix

- The confusion matrix is an important tool for evaluating the performance of classification models. This matrix is displayed as a 2x2 table and includes four main components:
- True Positives (TP): The number of positive samples that have been correctly identified.
- True Negatives (TN): The number of negative samples that have been correctly identified.
- False Positives (FP): The number of negative samples that have been incorrectly identified as positive.
- False Negatives (FN): The number of positive samples that have been incorrectly identified as negative.

Using this matrix, various metrics such as accuracy, precision, and recall can be calculated. Overall, the confusion matrix helps analysts identify the strengths and weaknesses of classification models and make better decisions for improving them (Powers 2020).

In this study, we investigated the accuracy of three different methods for identifying alterations, including Three-Dimensional Convolutional Neural Networks (3D-CNN), the combination of 3D-CNN and Support Vector Machines (SVM), and Three-Dimensional Wavelet Transform combined with SVM. The results obtained from the confusion matrices provide insight into the performance of these methods in classifying argillic, propylitic, and phyllic alterations.

Three-Dimensional Convolutional Neural Network (3D-CNN):

This method achieved an accuracy of 92%, as shown in the confusion matrix. The matrix indicates that the majority of predictions were correct, with only a few misclassifications. This suggests that the 3D-CNN effectively captures both spatial and spectral features from hyperspectral data, leading to accurate identification of alteration types.

Combination of 3D-CNN and SVM:

With an accuracy of 91%, this method demonstrates a strong performance as indicated by its confusion matrix. While the number of incorrect predictions is slightly higher than in the 3D-CNN method, the results still reflect a commendable capability in identifying alterations. The confusion matrix highlights the effectiveness of combining deep learning with support vector machines in improving classification accuracy.

Three-Dimensional Wavelet Transform and SVM:

This method recorded an accuracy of 89, indicating a decrease in performance compared to the previous two methods. The confusion matrix reveals some misclassifications, particularly in distinguishing between alteration types. Despite these errors, the method still successfully captures essential spatial and spectral features, though with slightly less precision.

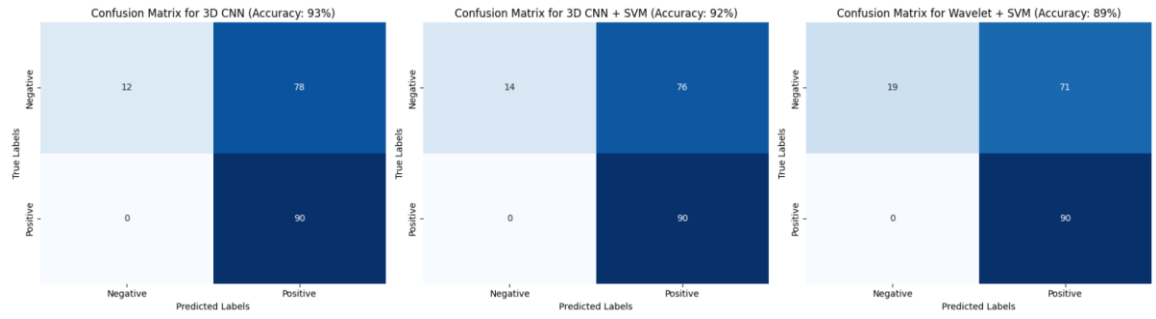

Figure 14: Confusion matrices illustrating the classification performance of three methods for identifying mineral alterations in hyperspectral data. The methods include: (a) Three-Dimensional Convolutional Neural Network (3D-CNN) with an accuracy of 92%, (b) Combination of 3D-CNN and Support Vector Machine (SVM) achieving an accuracy of 91%, and (c) Three-Dimensional Wavelet Transform combined with SVM, which yielded an accuracy of 89%. Each matrix highlights the number of correct and incorrect classifications for argillic, phyllic, and propylitic alteration types.

Kappa Statistic

The Kappa statistic (Kappa) is a statistical measure widely used to assess the agreement between two or more raters or measurement tools across various fields, particularly in medical and social sciences. This coefficient reflects the actual agreement between predictions and reality while accounting for the impact of chance agreement.(Ahmad, Khan et al. 2020)

The Kappa statistic is calculated as follows:

$$k = \frac{p_0 - p_e}{1 - p_e}$$

In this equation:

- p_0: represents the proportion of observed agreement (the observed agreement rate).
- $p_{e:}$ represents the proportion of expected agreement by chance (the expected agreement rate based on the frequencies of the categories).

Kappa values can range from -1 to 1. This measure assists researchers in quantitatively evaluating the accuracy and reliability of their measurement methods and interpreting the results more effectively. the Kappa coefficients for different methods are presented in Table 3.

Table 3: Overall accuracy, average accuracy, and Kappa coefficient for three different deep learning methods in identifying hydrothermal alteration zones.

Method	Overall accuracy(%)	Average accuracy(%)	Kappa× 100
3D CNN	93	92	86.60
3D CNN + SVM	92	91	84.80
3D Wavelet + SVM	89	87	80.83

III. CONCLUSIONS

In this study, deep learning methods based on spectral-spatial features were explored for identifying alteration zones in the Chehel Kureh copper deposit, one of the largest and richest copper mines in Iran. The methods investigated included 3D Convolutional Neural Networks (3D CNN), a combination of 3D CNN and Support Vector Machine (SVM), and a combination of 3D Wavelet Transform and SVM. The primary goal of this study was to assess the effectiveness of these methods in processing hyperspectral images and identifying mineralogical alterations associated with copper deposits.

The results from the experiments demonstrated that the 3D CNN method performed the best among the three approaches, achieving an overall accuracy of 92%. This method proved highly efficient in processing and analyzing spectral-spatial data, showcasing its high potential in mining exploration, particularly in identifying alteration zones that indicate copper mineralization.

Contrary to initial expectations, where it was anticipated that the combination of 3D CNN and SVM would yield higher accuracy, this combined method placed second with an overall accuracy of 91%. While the integration of these two methods showed promising results, it was slightly less effective than the standalone 3D CNN method. This suggests that, while combining SVM with 3D CNN holds potential, its performance does not significantly surpass that of 3D CNN alone, especially in detecting specific alteration zones in this mining area.

Additionally, the combined method of 3D Wavelet Transform and SVM exhibited lower performance compared to the other two methods, achieving an overall accuracy of 89%. This approach demonstrated weaker classification results, likely due to the added complexity introduced by the wavelet transformation process. Although wavelet transforms are useful for feature extraction in some cases, their integration with SVM may not have been as effective for spectral-spatial analysis, particularly considering the large and diverse data set derived from hyperspectral imagery.

When comparing the first two methods (3D CNN and 3D CNN+SVM), the accuracy scores were relatively close. Both methods performed well in detecting overlapping alteration zones, demonstrating their ability to handle complex spatial information. However, in identifying propylitic alteration zones, the 3D CNN method outperformed the 3D CNN+SVM combination, showing this alteration type with greater precision. In contrast, both methods performed similarly in detecting argillic and phyllic alterations, which are typically more subtle and less distinct.

These findings highlight the ability of the 3D CNN method to effectively process hyperspectral images for alteration zone identification, making it an effective tool in this field. This research also emphasizes the importance of increased attention to the Chehel Kureh region in future studies, as it presents significant potential for further exploration and

research. The region remains an important copper resource, and enhancing the accuracy of alteration zone identification methods can lead to more efficient exploration and extraction processes.

IV. REFERENCES

[1] Berberian, F. and M. Berberian (1981). "Tectono-plutonic episodes in Iran." Zagros Hindu Kush Himalaya Geodynamic Evolution **3**: 5-32.

[2] Camp, V. and R. Griffis (1982). "Character, genesis and tectonic setting of igneous rocks in the Sistan suture zone, eastern Iran." Lithos **15**(3): 221-239.

[3] Delaloye, M. and J. Desmons (1980). "Ophiolites and mélange terranes in Iran: a geochronological study and its paleotectonic implications." Tectonophysics **68**(1-2): 83-111.

[4] Maanijou, M. (2007). "Geochemistry, origin of ore fluids, and formation of Chehelkureh copper deposit (NW of Zahedan)." Ph. D. Thesis: 236.

[5] Maanijou, M., et al. (2008). "Petrography and alteration of Chehelkureh copper deposit: Mass balance of elements and behavior of REE." Scientific Quarterly Journal of Geosciences **17**(67): 86-101.

[6] Maanijou, M., et al. (2009). "MINERALOGRAPHY, AND EPMA STUDY OF SULFIDE MINERALS IN CHEHELKUREH ORE DEPOSIT, ZAHEDAN, SE IRAN".

[7] Stöcklin, J., et al. (1972). Central lut reconnaissance east iran, geological survey of iran, Report.

[8] Tirrul, R., et al. (1983). "The Sistan suture zone of eastern Iran." Geological Society of America Bulletin **94**(1): 134-150.

[9] Ahmad, M., et al. (2020). "A fast and compact 3-D CNN for hyperspectral image classification." IEEE Geoscience and Remote Sensing Letters **19**: 1-5.

[10] Anand, R., et al. (2021). "Robust classification technique for hyperspectral images based on 3D-discrete wavelet transform." Remote Sensing **13**(7): 1255.

[11] Bedini, E. and J. Chen (2020). "Application of PRISMA satellite hyperspectral imagery to mineral alteration mapping at Cuprite, Nevada, USA." Journal of hyperspectral remote sensing v **10**(2): 87-94.

[12] Bera, S., et al. (2022). "Advances in Hyperspectral Image Classification Based on Convolutional Neural Networks: A Review." CMES-Computer Modeling in Engineering & Sciences **133**(2).

[13] Berberian, F. and M. Berberian (1981). "Tectono-plutonic episodes in Iran." Zagros Hindu Kush Himalaya Geodynamic Evolution **3**: 5-32.

[14] Camp, V. and R. Griffis (1982). "Character, genesis and tectonic setting of igneous rocks in the Sistan suture zone, eastern Iran." Lithos **15**(3): 221-239.

[15] Cao, X., et al. (2020). "Hyperspectral image classification with convolutional neural network and active learning." IEEE Transactions on Geoscience and Remote Sensing **58**(7): 4604-4616.

[16] Chen, Y., et al. (2020). Efficient 3D neural networks with support vector machine for hippocampus segmentation. 2020 international conference on artificial intelligence and computer engineering (ICAICE), IEEE.

[17] Delaloye, M. and J. Desmons (1980). "Ophiolites and mélange terranes in Iran: a geochronological study and its paleotectonic implications." Tectonophysics **68**(1-2): 83-111.

[18] Esmaeili, M., et al. (2024). "PRISMA hyperspectral imagery for mapping alteration zones associated with Kuhpanj porphyry copper deposit, Southern Iran." European Journal of Remote Sensing **57**(1): 2299369.

[19] Fu, Y., et al. (2023). "Mineral prospectivity mapping of porphyry copper deposits based on remote sensing imagery and geochemical data in the Duolong ore district, Tibet." Remote Sensing **15**(2): 439.

[20] Graham, G. E., et al. (2018). "Application of imaging spectroscopy for mineral exploration in Alaska: A study over porphyry Cu deposits in the eastern Alaska Range." Economic geology **113**(2): 489-510.

[21] Habashi, J., et al. (2024). "PRISMA hyperspectral remote sensing data for mapping alteration minerals in sar-e-châh-e-shur region, Birjand, Iran." Remote Sensing **16**(7): 1277.

[22] Harraden, C. L., et al. (2013). "Shortwave infrared spectral analysis of hydrothermal alteration associated with the Pebble porphyry copper-gold-molybdenum deposit, Iliamna, Alaska." Economic geology **108**(3): 483-494.

[23] Heller Pearlshtien, D., et al. (2021). "PRISMA sensor evaluation: A case study of mineral mapping performance over Makhtesh Ramon, Israel." International Journal of Remote Sensing **42**(15): 5882-5914.

[24] Li, N., et al. (2024). "Discriminating Spectral–Spatial Feature Extraction for Hyperspectral Image Classification: A Review." Sensors **24**(10): 2987.

[25] Li, Y., et al. (2017). "Spectral–spatial classification of hyperspectral imagery with 3D convolutional neural network." Remote Sensing **9**(1): 67.

[26] Loizzo, R., et al. (2019). Prisma mission status and perspective. IGARSS 2019-2019 IEEE International Geoscience and Remote Sensing Symposium, IEEE.

[27] Lowell, J. D. and J. M. Guilbert (1970). "Lateral and vertical alteration-mineralization zoning in porphyry ore deposits." Economic geology **65**(4): 373-408.

[28] Maanijou, M. (2007). "Geochemistry, origin of ore fluids, and formation of Chehelkureh copper deposit (NW of Zahedan)." Ph. D. Thesis: 236.

[29] Maanijou, M., et al. (2008). "Petrography and alteration of Chehelkureh copper deposit: Mass balance of elements and behavior of REE." Scientific Quarterly Journal of Geosciences **17**(67): 86-101.

[30] Maanijou, M., et al. (2009). "MINERALOGRAPHY, AND EPMA STUDY OF SULFIDE MINERALS IN CHEHELKUREH ORE DEPOSIT, ZAHEDAN, SE IRAN."

[31] Neal, L. C., et al. (2018). "Spectral characteristics of propylitic alteration minerals as a vectoring tool for porphyry copper deposits." Journal of Geochemical Exploration **184**: 179-198.

[32] Peyghambari, S., et al. (2024). "One-Dimensional-Mixed Convolution Neural Network and Covariance Pooling Model for Mineral Mapping of Porphyry Copper Deposit Using PRISMA Hyperspectral Data." Photogrammetric Engineering & Remote Sensing **90**(8): 511-522.

[33] Powers, D. M. (2020). "Evaluation: from precision, recall and F-measure to ROC, informedness, markedness and correlation." arXiv preprint arXiv:2010.16061.

[34] Praveen, B. and V. Menon (2020). "Study of spatial–spectral feature extraction frameworks with 3-D convolutional neural network for robust hyperspectral imagery classification." IEEE Journal of selected topics in applied earth observations and remote sensing **14**: 1717-1727.

[35] Sillitoe, R. H. (2010). "Porphyry copper systems." Economic geology **105**(1): 3-41.

[36] Singer, D. A. (2017). "Future copper resources." Ore Geology Reviews **86**: 271-279.

[37] Sorrentino, A., et al. (2024). "The application of PRISMA hyperspectral satellite imagery in the delineation of distinct hydrothermal alteration zones in the Chilean Andes: The Marimaca IOCG and the Río Blanco-Los Bronces Cu-Mo porphyry districts." Ore Geology Reviews: 105998.

[38] Spiller, D., et al. (2023). "Wildfire Detection Using Convolutional Neural Networks and PRISMA Hyperspectral Imagery: A Spatial-Spectral Analysis." Remote Sensing **15**(19): 4855.

[39] Stöcklin, J., et al. (1972). Central lut reconnaissance east iran, geological survey of iran, Report.

[40] Tirrul, R., et al. (1983). "The Sistan suture zone of eastern Iran." Geological Society of America Bulletin **94**(1): 134-150.

[41] Wu, G., et al. (2024). "Hyperspectral image classification using graph convolutional network: A comprehensive review." Expert Systems with Applications **257**: 125106.

[42] Zhang, B., et al. (2020). "Three-dimensional convolutional neural network model for tree species classification using airborne hyperspectral images." Remote Sensing of Environment **247**: 111938.